



Contents lists available at ScienceDirect

Journal of Wind Engineering & Industrial Aerodynamics

journal homepage: www.elsevier.com/locate/jweia

Identification of flow classes in the wake of a simplified truck model depending on the underbody velocity



Thomas Castelain^{a,c,*}, Marc Michard^a, Mathieu Szmigiel^{a,b}, Damien Chacaton^b, Daniel Juvé^a

^a Université de Lyon, École Centrale de Lyon and LMFA UMR CNRS 5509, F-69134, Ecully, France

^b Volvo Group Truck Technology, Renault Trucks SAS, Cab Engineering Lyon, 99 route de Lyon, 69806, Saint-Priest Cedex, France

^c Université de Lyon, Université Lyon 1 and LMFA UMR CNRS 5509, F-69622, Villeurbanne, France

ARTICLE INFO

Keywords:

Aerodynamics
Experiments
Ground effect
Road vehicles
Wake

ABSTRACT

An experimental study of the near wake of a simplified truck model with an aspect ratio between the height and the width greater than one is presented. The influence of the underbody velocity at a constant ground clearance height is considered. The evolution of the model base pressure and of the near wake as a function of the underbody velocity permits to identify four classes of flow. For large values of underbody velocity, typically above 60% of the free stream velocity, the near-wake structure is similar to what obtained in bluff-body characterizations where the underbody flow momentum is sufficient to prevent its detachment from the ground. For smaller values of underbody velocity, of particular interest when considering real truck applications, base pressure mean value and near wake characteristics strongly depend on the underbody velocity; three different classes are defined through the values of time-averaged rear pressure as well as a qualitative analysis of the near-wake structure. Quantitatively, a momentum budget in the near-wake together with the characterization of the curvature of the underbody flow near the model end provide ad-hoc indicators for discriminating between the different flow classes.

1. Introduction

Medium and heavy duty vehicles can be considered as square-back bluff-bodies with an aspect ratio between their height H and width W above one. Depending on the practical use of the vehicle, the ground clearance height of the cab and the free space under the trailer can vary. This leads to various flow blockages in the underbody area and results in different wake topologies. The possible energy gains linked with a better understanding of the physical phenomena related to drag forces motivated studies at industrial scales. For instance, results on van-type vehicles (Bonnavion et al., 2017) confirmed the occurrence of multistability on such a configuration, as previously obtained on a Ahmed body at industrial-scale (Grandemange et al., 2015). At smaller scale or for academic studies, simplified models of medium and heavy duty vehicles are used, among which simplified reduced-scale models of a real heavy duty vehicle, preserving the main aerodynamically significant details (simplified cooling system, indicators and vehicle registration holder plate for instance) (Hwang et al., 2016; Salati et al., 2017), or more simplified models such as the Ground Transportation System (GTS) or the Generalized European Transport System (GETS) (Croll et al., 1996;

Gutierrez et al., 1996; McArthur et al., 2016; Storms et al., 2001; Van Raemdonck and Van Tooren, 2008). For these models, consisting of a rounded nose coupled with an elongated parallelepiped shape of aspect ratio $H/W > 1.3$, the ground clearance G is also a parameter of the experimental set-up, and governs the balance between the free stream and the underbody flow. When $G^* = G/H \geq 0.14$, the bulk underbody flow velocity is very close to the free stream velocity (Croll et al., 1996; Gutierrez et al., 1996; Islam et al., 2017; Storms et al., 2001; Van Raemdonck and Van Tooren, 2008); the mean near wake is then composed of a closed recirculation bubble detached from the ground. From a qualitative point of view in this case, the wake structure is reminiscent of that obtained in passenger vehicles studies based on the Ahmed body (Ahmed et al., 1984), Windsor (Littlewood and Passmore, 2012) or ASMO models (Nakashima et al., 2008). Nevertheless, for full-scale trucks, the underbody bulk velocity ranges from 10% to 40% of the free stream velocity. As a consequence, the wake develops closer to the ground because of the limited momentum flux from the underbody flow. Previous studies already tackled the issue of handling the underbody velocity value, or proposed systems that could serve this purpose. A slanted underbody rear geometry was added by Kowata et al. (2008) to a

* Corresponding author. Université de Lyon, Université Lyon 1 and LMFA UMR CNRS 5509, F-69622, Villeurbanne, France.

E-mail address: thomas.castelain@ec-lyon.fr (T. Castelain).

<https://doi.org/10.1016/j.jweia.2018.02.004>

Received 29 September 2017; Received in revised form 8 February 2018; Accepted 10 February 2018

Nomenclature	
$\bar{\bullet}$	Time-average value of \bullet
$\langle \bullet \rangle$	Spatial-average value of \bullet
\bullet'	Fluctuating part of \bullet
σ_{\bullet}	Standard deviation of \bullet
\bullet^*	Length \bullet normalized by H , or velocity component \bullet normalized by U_{∞}
U_{∞}	Free stream velocity
u, v, w	Velocity components in the reference frame
U	Velocity magnitude in the longitudinal plane
U_s	Bulk underbody velocity
λ	Ratio between U_s and U_{∞}
k^*	Turbulent kinetic energy normalized by U_{∞}^2
H, W, L	Model Height, Width, Length
ν	Air kinematic viscosity
Re_H	Reynolds number based on U_{∞} and H
ϕ	Porosity of pressure loss system

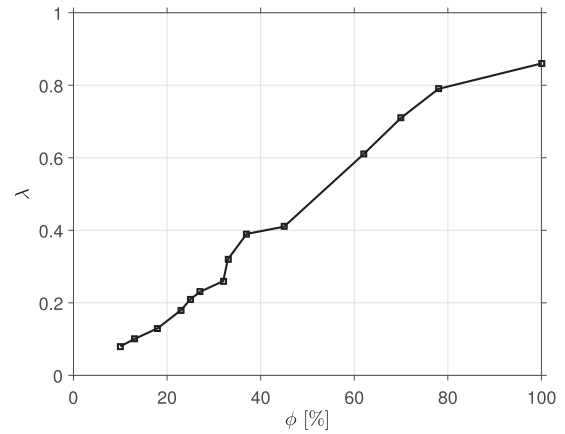


Fig. 3. Evolution of the ratio $\lambda = U_s/U_{\infty}$ with the porosity.

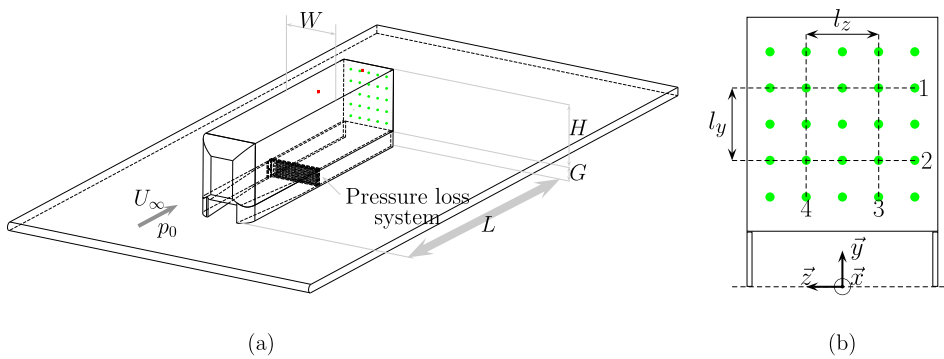


Fig. 1. Experimental set-up: (a) perspective view, (b) rear view. Locations of base pressure taps are given by \bullet ; those on the roof by \blacksquare . The pressure loss system is not represented in (b).

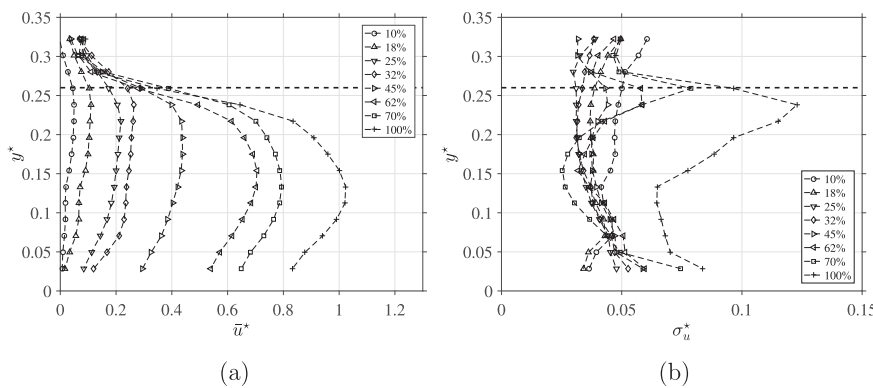


Fig. 2. Profiles at $x^* = 0.02$ of (a) normalized mean longitudinal velocity and (b) standard deviation of the underbody flow for several pressure losses. Each symbol in the legend corresponds to a value of porosity ϕ ; the black dashed line represents the ground clearance top.

square-back Ahmed body for drag reduction. Varying the angle of the slanted part would result in changing the underbody velocity at the model exit, but would consequently modify the height of the model rear. Perry and Passmore (2013) introduced roughness in the underbody area of a square-back Windsor model, which led to an underbody velocity change due to the induced pressure losses. To some extent, whether the ground displacement is reproduced or not can also influence the underbody bulk velocity, as a consequence of changes in the flow boundary condition on the ground; Garry (1996) for instance measured the base pressure of simplified bluff bodies with $H/W > 1$ for various ground

plane velocities ranging from 0 to U_{∞} , and Krajnovic et al. (Krajnovic and Davidson, 2015) showed that the influence of the floor motion on the wake structure of a slanted surface body is qualitatively limited to the region near the floor and near the slanted surface. Finally, the ground clearance can be decreased to reduce the underbody velocity, because of the enhancement of pressure losses in the underbody area.

Barros et al. (2016) showed that, for a body of simplified geometry and with flow control, a strong connection exists between the change in base pressure and the drag evolution as a function of the actuation parameters. Grandemange et al. (2013a) studied the effect of ground

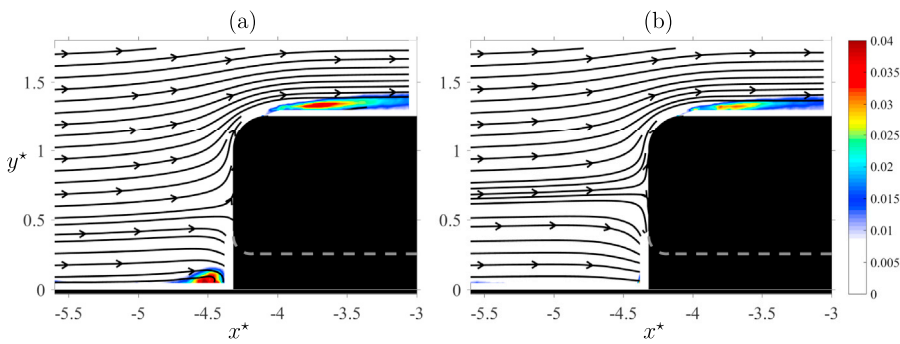


Fig. 4. Mean velocity streamlines superimposed with the maps of the normalized turbulent kinetic energy in the mid plane for $\lambda = 0.08$ (a) and $\lambda = 0.86$ (b). The dashed line is the limit of the ground clearance area.

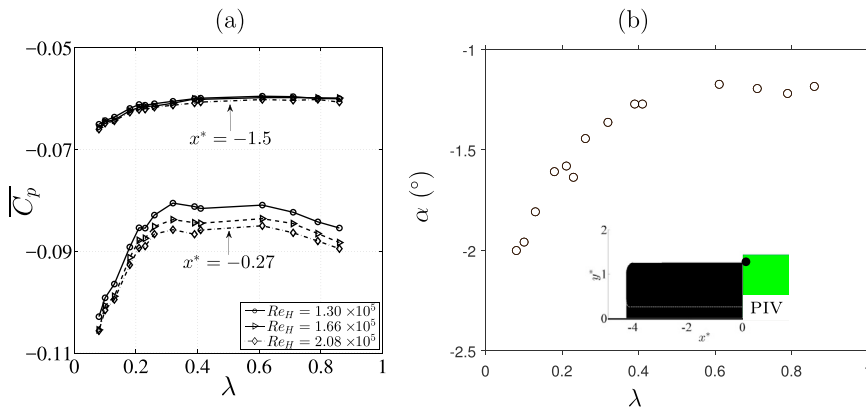


Fig. 5. Evolution with λ of (a) the mean pressure coefficient for several Reynolds numbers at $x^* = -1.5$ and at $x^* = -0.27$; (b) the streamline local angle with respect to \vec{x} direction, at the reference point \bullet located at $(x^*, y^*) = (0.06, 1.35)$.

clearance variations on the near wake of square-back bodies of different aspect ratios, including $H/W = 1.34$. There is no simple relationship between the mean base pressure (and drag, following (Barros et al., 2016)) and ground clearance velocity. A marked effect on mean base pressure, and drag, is obtained as G^* varies. A minimum of the mean base pressure is reached for $G/W \approx 0.06$ (thus $G^* \approx 0.045$). This value, independent of H/W , is identified as 'the transition from a backward facing step topology to a common wake topology of a simplified vehicle'. Unfortunately, velocity fields for $H^* > 1$ are not provided. Furthermore, McArthur et al. (2016) changed progressively the ground clearance height for the GTS model, and characterized the wake for $G^* \approx 0.14$ down to 0.03 by use of PIV measurements. Three different wake topologies were noticed in addition to that obtained for $G^* \approx 0.14$ or higher, which is consistent with previous results (Szmigiel et al., 2016) obtained on a reduced-scale model of an industrial vehicle with flaps where 4 wake topologies were illustrated. In these different studies (Grandemange et al., 2013a; McArthur et al., 2016), the evolution of the near wake characteristics results from the combined effects of the variation of two physical parameters simultaneously. By varying the ground clearance height, viscous effects take place that limit the underbody flow momentum; the effect of the floor proximity is also modified.

The objectives of the present study are threefold: (i) determine the evolution of the near wake characteristics as the underbody flow momentum is modified while the ground clearance height is kept constant, (ii) investigate the possibility to classify these different wake structures using indicators derived from flow measurements, (iii) compare the identified flow classes to those obtained by changing the ground clearance height (Grandemange et al., 2013a; McArthur et al., 2016). Here, a simplified square-back truck model is studied. The influence of the underbody velocity on the near-wake characteristics and on the base pressure is investigated, with a ground clearance fixed to $G^* = 0.25$. The experimental set-up is described in Section 2 together with the measurement techniques and the procedure to determine the underbody bulk

velocity. The flow characteristics around the model are presented in Section 3. The base pressure distribution, the near-wake structure in terms of time-averaged velocity fields and the associated Reynolds stresses distribution are given in Section 4. Analyses based on a momentum budget, the evaluation of the underbody flow curvature in the near wake and base pressure gradients provide results compared in Section 5 to those derived from base pressure measurements.

2. Experimental set-up and underbody flow characterization

2.1. Low-scale tractor-trailer model

Experiments are carried out at École Centrale de Lyon, LMFA, in an open wind tunnel where the flow exhausts from a 500 mm-side square section. A simplified tractor-trailer model of scale 1:43 with a 90° rear slant angle, presented in Fig. 1, is studied. The length L of the bluff body is 320 mm, its height H and width W are respectively 74 mm and 66 mm. The aspect ratio H/W is thus equal to 1.12, which corresponds to a classical value encountered in European long haul vehicles. The ground clearance height G is 19 mm so that $G^* = 0.25$ is identical to that of previous studies at larger scale (Chaligné, 2013) and close to the value of full scale long haul vehicle. The model is positioned on a flat plate, 133 mm downstream its leading edge. Results have been obtained for a free stream velocity U_∞ set to 25 m s^{-1} leading to a Reynolds number $Re_H = U_\infty H / \nu = 1.3 \times 10^5$. In some cases U_∞ was fixed to 32 m/s and 40 m/s to investigate the influence of Re_H . The peculiarities of this model are twofold: its aspect ratio and the presence of side skirts. The side skirts, fixed on the ground without gap, are used to channel the underbody flow which is forced to pass through a pressure loss system located in the ground clearance, 160 mm downstream of the model front. The effect on body drag of the side skirts, known from previous works (Hwang et al., 2016) to be beneficial in heavy trucks configurations, is not considered here but their presence is mandatory to allow for the management of the

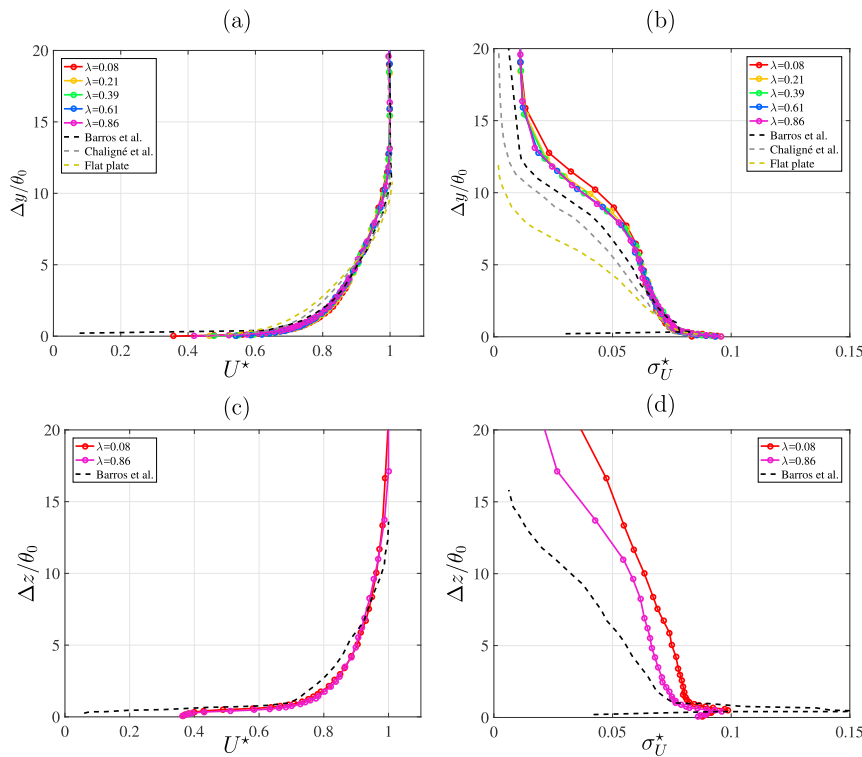


Fig. 6. Profiles of normalized mean velocity magnitude and standard deviation at $x^* = -0.07$ in the mid plane (a,b) and at mid height on the side of the model (c,d). Comparison with results from (Chaligné, 2013; Barros et al., 2016; Klebanoff, 1955).

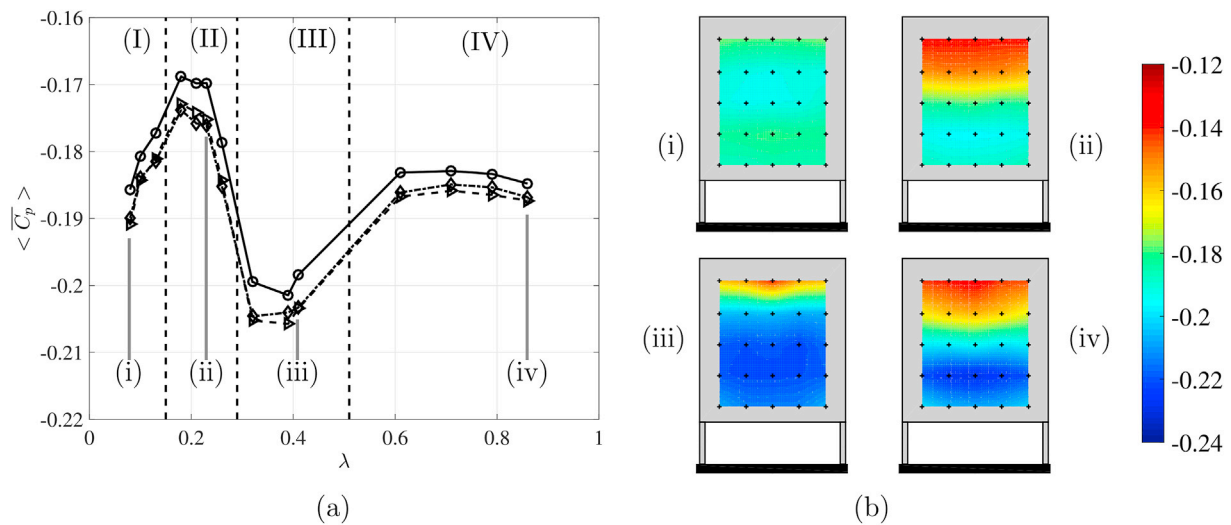


Fig. 7. (a) Evolution of the mean base pressure coefficient $\langle \overline{C_p} \rangle$ with λ for three Re_H values (\circ) 1.30×10^5 , (\triangle) 1.66×10^5 , (\diamond) 2.08×10^5). (b) Maps of $\overline{C_p}$ on the rear surface for selected values of $\lambda =$ (i) 0.08, (ii) 0.21, (iii) 0.39, (iv) 0.86.

underbody flux at constant ground clearance height. The pressure loss device, depicted in Fig. 1(a), is made of a 4 mm thick grid with a porosity ϕ adjustable between 10% and 100% of the ground clearance area. This allows for the underbody velocity to be adjusted without modifying the ground clearance height. To minimize flow separation on the upstream part of the model, a rounded shape of the model nose has been chosen. The choice of the radius for the upper and lateral edges equal to 19 mm and for the lower edge equal to 9 mm results from a previous study (Chaligné, 2013). A 5 mm-large sandpaper band of 25 μm grains is placed just after the nose on the roof and the side walls to help the transition of the boundary layers. The coordinate system is defined as the x axis directed toward the flow direction, y normal to the ground and z forming a direct trihedral. The origin of the coordinate system is defined as the

point on the flat plate at the mid-span and rear end of the model. The three components of the velocity are noted u , v and w , respectively associated to the \vec{x} (streamwise), \vec{y} (vertical) and \vec{z} (spanwise) direction.

2.2. Measurement techniques

2.2.1. Pressure measurements

Two wall pressure taps are located on the roof and 25 taps are distributed on the model base as depicted in Fig. 1. The pressure is measured using a 32-port ESP pressure scanner of 0–1000 Pa full scale interfaced to a μDAQ located outside the model. The scanner is linked to

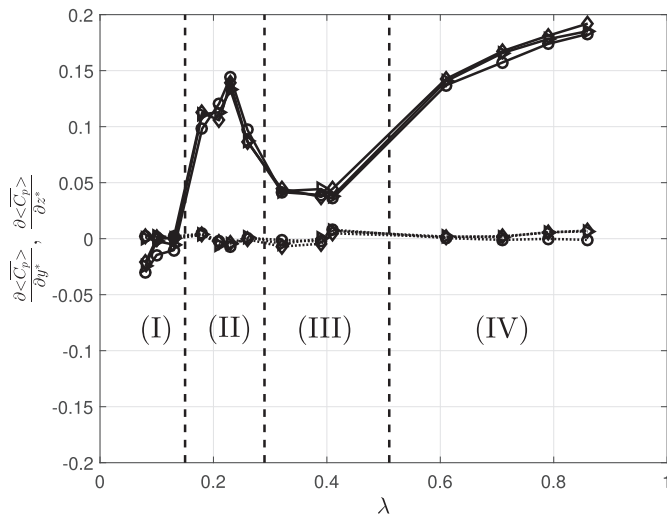


Fig. 8. Evolution of the vertical (solid lines) and horizontal (dashed lines) pressure gradients with λ for three Re_H values (see caption of Fig. 7).

each tap by tubes 270 mm long. To prevent flow disturbances, communicating wires for data transfers between the pressure scanner and the μ DAQ are inserted inside the skirts. The acquisition frequency rate is set to 1 kHz. The frequency response of this set-up has been tested independently and can be considered as flat up to 400 Hz which is significantly above the bandwidth of interest here. The dimensionless pressure coefficient C_p is defined by use of the upstream static pressure p_0 and the air density ρ :

$$C_p = (p - p_0) / (1/2 \rho U_\infty^2) \tag{1}$$

2.2.2. Hot-wire probe

A Dantec Dynamics 55P01 hot-wire probe, associated with a Dantec Dynamics Streamline 90N10 anemometer, is mounted on a displacement system to characterize the boundary layers developing along the roof and side walls and to perform spectral analysis in the near wake. For boundary layer measurements, signals are sampled at 12.8 kHz during 10 s.

2.2.3. Particle image velocimetry

Study of the front flow is carried out by using 2D2C particle image velocimetry (PIV). The whole wake in the mid plane and the wake in the transversal plane at $x^* = 0.5$ are characterized by using stereoscopic PIV (SPIV). The laser system is a Nd:YAG Quantronix Darwin Duo of 2×18 mJ. The laser head is installed above the flow. The cameras used are CMOS Phantom V12 having a resolution of 1280×800 pixels. For SPIV, the cameras are placed on each side of the mid plane and inclined by an angle of 41° with respect to the direction of the upstream flow. The acquisition frequency rate of image pairs is set to 100 Hz. For each

measurement, 1000 image pairs are recorded. Image processing is performed with DaVis 7.2.2 software using interrogation windows of decreasing size from 64×64 pixels down to 16×16 pixels and an overlap of 50%. The final grid resolution is 1.53 mm for the front flow, 0.99 mm for the whole wake in the mid plane and 1.08 mm for the transversal plane, this last value corresponding to 0.015 H.

2.3. Underbody velocity characterization

The flow at the underbody exit is investigated using SPIV, to determine the influence of porosity ϕ of the pressure loss system on the underbody flow homogeneity and evaluate the underbody bulk velocity for each value of ϕ . Vertical profiles of velocity \bar{u} at $x^* = 0.02$ in the mid-plane are given in Fig. 2(a) for selected grids over the investigated range of porosity. These profiles are rather symmetrical with respect to the middle of the ground clearance ($y^* = 0.13$), as expected for a channel flow; the slight deviation from symmetry, in particular for low values of ϕ , may be attributed to differences in the boundary layers development along the ground ($y^* = 0$) and along the model bottom ($y^* \approx 0.26$). Profiles of velocity fluctuations are provided in Fig. 2(b). For $\phi \geq 62\%$ the maximum of velocity fluctuations is located in the shear layer downstream the underbody exit. Furthermore, the turbulence level within the ground clearance flow is rather constant as long as the pressure loss system is used ($\phi < 100\%$). This level is higher in the case $\phi = 100\%$. The bulk underbody flow velocity U_s is evaluated by integrating the vertical profiles of \bar{u} (Fig. 2(a)) over the ground clearance height. The evolution of the dimensionless parameter $\lambda = U_s/U_\infty$ with ϕ is presented in Fig. 3. The evolution of λ is roughly linear in the range $\phi \in [10\%:80\%]$. Without underbody grid ($\phi = 100\%$), one may have expected λ to reach 1 ($U_s \approx U_\infty$); a smaller value is obtained ($\lambda = 0.85$), which is attributed to the combined effects of residual head losses in the ground clearance area, of the incoming boundary layer which develops over the ground and of a potential effect of the body in ground proximity. This last effect limits the velocity magnitude upstream of the body in a region of typical longitudinal size H ; the boundary layer limits the velocity magnitude near the ground. This results in a deficit of bulk velocity in the model underbody with respect to the freestream velocity U_∞ even in the case $\phi = 100\%$.

3. Flow around the model

After having considered the bulk underbody flow velocity obtained by use of grids of different porosity in the underbody area, we describe the flow around underbody entrance at the model front, and on the model sides, where the influence of the pressure loss device is expected to be moderate.

3.1. Flow upstream of the model

The flow upstream of the body is first studied, by use of PIV in the mid plane for two underbody configurations $\lambda = 0.08$ and $\lambda = 0.86$. This last configuration is the reference case with no pressure loss grid in the

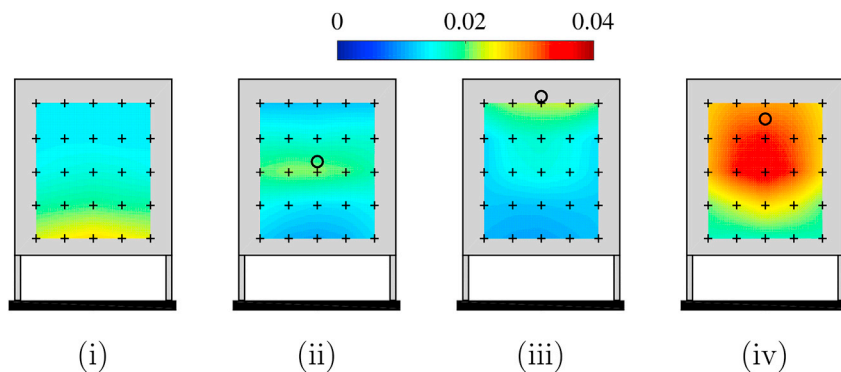


Fig. 9. Color maps of standard deviation values of C_p for selected values of λ : (i) 0.08, (ii) 0.21, (iii) 0.39, (iv) 0.86. The crosses indicate wall pressure taps and the black circles symbolize the stagnation points identified in section 4.2. (For interpretation of the references to color in this figure legend, the reader is referred to the Web version of this article.)

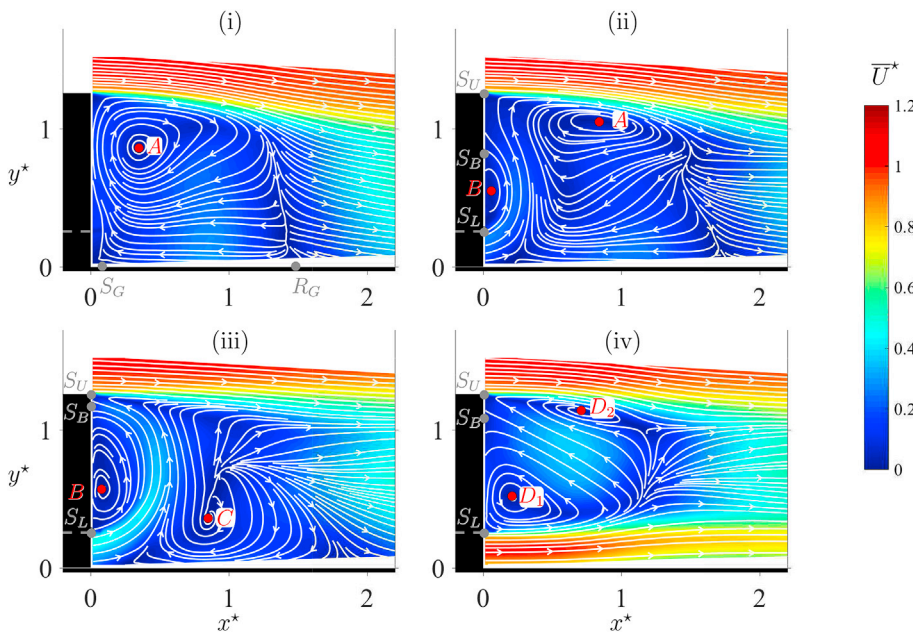


Fig. 10. Non-dimensional mean velocity magnitude in the mid plane for selected values of λ : (i) 0.08, (ii) 0.21, (iii) 0.39, (iv) 0.86.

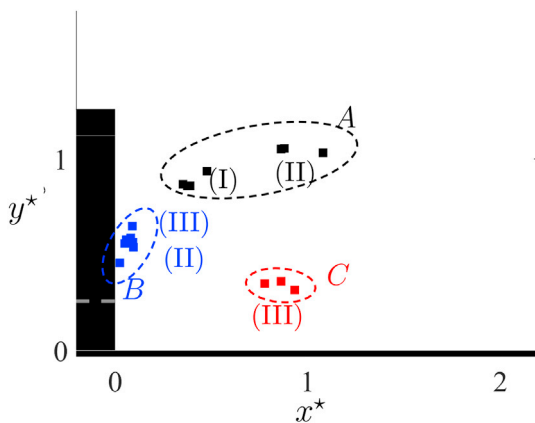


Fig. 11. Locations of the vortex centers detected in the mid-plane velocity field, for the different values of λ tested.

underbody area, while the case $\lambda = 0.08$ corresponds to the maximum pressure loss which is most susceptible to change the flow characteristics around the model. In Fig. 4, the streamlines of the time averaged velocity field together with the normalized two component turbulent kinetic energy k^* are given. The stagnation point moves towards the middle of the model nose when λ increases, as a result of a better balance between the underbody velocity and the free stream velocity. For $\lambda = 0.08$ and up to $\lambda = 0.18$, significant levels of velocity fluctuations are located in a small area near the ground, upstream of the underbody entrance where a local curvature of the streamlines is visible. In this case, the grid porosity is so small that the very limited underhood flux makes the model behave like a surface-mounted obstacle. The flow behavior around a sharp-edge surface-mounted obstacle has been previously studied (for parallelepiped obstacles in (Basara, 2015; Martinuzzi and Tropea, 1993) or cylinders (Uffinger et al., 2013) for instance), which highlighted the existence of a horseshoe vortex in the vicinity of the surface. A careful examination of the time-averaged velocity field (not provided here) confirmed here the presence of a vortical structure upstream of the ground clearance entrance. The velocity fluctuations upstream of the underbody entrance come from small variations of the location of this horseshoe vortex.

Furthermore, intermittent flow separation at the model nose induces

high level of k^* over the model top. When λ decreases from 0.86 down to 0.08, the maximum of k^* on the roof increases by 15%; the area where k^* is larger than 0.01 above the model roof is not affected by the change in λ . Thus, the main features of k^* at the model front in the symmetry plane weakly depend on λ . To complement this first analysis, the wall pressure on the roof and the boundary layers on the model sides are now presented.

3.2. Wall pressure on the roof

A further assessment of the flow conditions downstream of the model nose is given by the wall pressure measurements on the roof at $x^* = -1.5$ as illustrated in Fig. 5(a). This point is located at $2L/3$ downstream of the model front. The time averaged wall pressure is independent of Re_H and is very weakly dependent of λ , which tends to indicate that the flow modifications over the model roof downstream the nose (see section 3.1) have limited effects on the flow around the downstream part of the model. For the results obtained at $x^* = -0.27$, thus very close to the model rear end, a dependency of $\overline{C_p}$ with λ is noticeable in Fig. 5(a). $\overline{C_p}$ increases with λ up to $\lambda = 0.3$, after which the value of the pressure coefficient remains nearly constant. At this location over the model roof, the time-averaged pressure can be affected by the modifications brought to the near-wake structure by a change in λ . To illustrate this effect, the orientation of the streamlines above the model rear end is presented in Fig. 5(b), using the velocity maps obtained by PIV. Different streamlines are considered in a region centered around the reference point located just behind the model rear and just above the shear layer where the velocity fluctuations are small, at position $(x^*, y^*) = (0.06, 1.35)$. The curvature of the streamlines is small in this region, and the angle α between the local streamline and the \vec{x} axis has thus a value of only a few degrees. A spatial average over $0.067H$ centered around the reference point is performed and the estimated accuracy of the evaluation of α from the time-averaged streamlines is 0.05° ; as a complement, the robustness of the trend for the evolution of α with λ has been tested against small variations of the location of the reference point. Under the reasonable assumption that these streamlines are oriented strictly along the \vec{x} axis above the model (thus $\alpha = 0^\circ$ there), any change in the streamline orientation near the model end should come from a streamline curvature, which is associated with a reduction of pressure in this area. Analyzing the behavior of the evolution of α with λ in Fig. 5(b) indicates that the

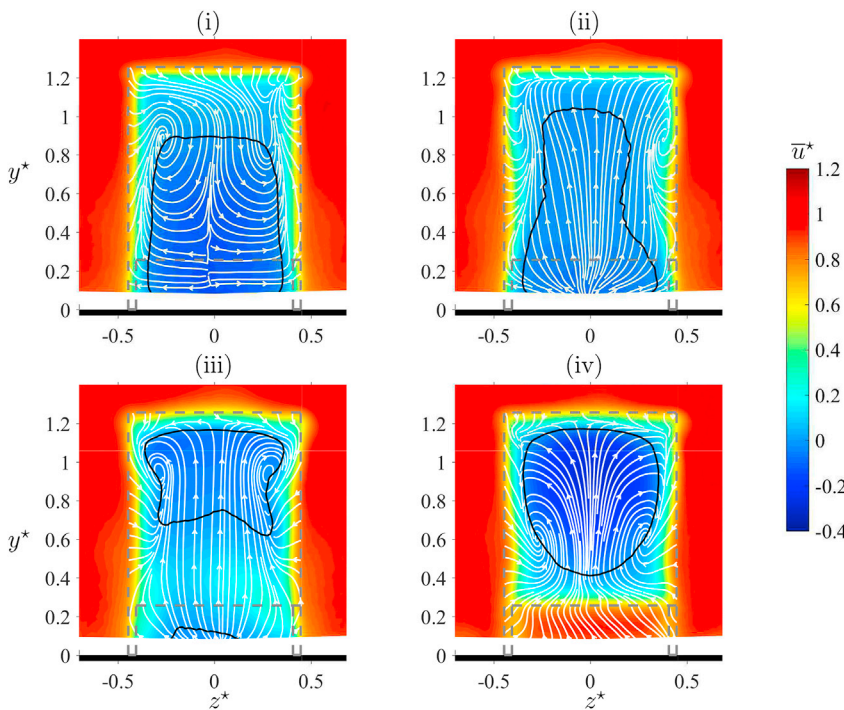


Fig. 12. Streamlines and mean streamwise velocity in a transversal plane at $x^* = 0.5$ for $\lambda =$ (i) 0.08, (ii) 0.21, (iii) 0.39, (iv) 0.86. The isoline $u^* = 0$ is superimposed on each map.

corresponding radius of curvature tends to increase up to $\lambda = 0.3$ and is nearly constant above this value. This is fully consistent with the evolution of $\overline{C_p}$ measured near the model rear end.

3.3. Boundary layer characteristics

Hot wire measurements carried out upstream the model rear end are now considered. Mean velocity profiles and standard deviation profiles at $x^* = -0.07$ in the mid plane are presented in Fig. 6(a and b). Normalized profiles from hot-wire measurements, on a flat plate with no pressure gradient (Klebanoff, 1955) and from a model similar to the one used in the present study but at a larger scale (Chaligné, 2013) or another model with a smaller aspect ratio H/W (Barros et al., 2016), are recalled for comparison. Considering the differences in characteristics of these various models (in particular, their length and aspect ratios), the fact that they have been tested in different wind tunnels, the turbulence levels measured from hot-wire surveys are likely not to be identical. Nevertheless, this difference in levels apart, the evolutions of the velocity fluctuations with the normal coordinate follow comparable trends. The boundary layer is turbulent for the three model walls in the downstream part of the model, as depicted by the velocity profiles and confirmed by integral parameters of these boundary layers provided in Appendix A. The influence of λ on the profiles is small with respect to the differences with reference profiles. These differences consist essentially in a slightly higher level of velocity fluctuations in the outer part of the boundary layer ($\Delta y/\theta_0 \approx 10$ typically, with θ_0 the local momentum thickness) for the measurements on models with respect to flat plate measurement. This may result from an intermittent flow separation downstream the model nose as pointed out in section 3.1. The velocity profiles on one side of the model, at mid-height, are also considered and presented in Fig. 6(c and d). The time-averaged velocity profile is similar to that obtained over the model roof. Velocity fluctuations are slightly higher in this case, in particular for $\lambda = 0.08$, which may be linked with the convection of the disturbances depicted in Fig. 4(a).

These first results indicate that the influence of λ on the flow over the model roof and the sides is limited. This ensures clean test conditions for the wake study in the different conditions of blockage ratio in the underbody area.

4. Near wake

4.1. Rear base pressure

The evolution with λ of the spatially averaged base pressure coefficient $\langle \overline{C_p} \rangle$ is given in Fig. 7(a), for three test configurations corresponding to different values of Reynolds number Re_H . The global trend of $\langle \overline{C_p} \rangle$ with λ is very slightly affected by a change in Re_H , within the range of Re_H tested. Below $\lambda = 0.61$, the base pressure is highly sensitive to λ . For very low underbody velocities, $\langle \overline{C_p} \rangle$ sharply increases with λ up to a maximum for $\lambda \approx 0.2$; for λ above 0.2, a marked decrease of $\langle \overline{C_p} \rangle$ with λ is noticed up to a minimum value for $\lambda = 0.4$. Finally, for λ above 0.4, the base pressure coefficient increases and reaches a plateau. For a given ratio H/W of a square-back Ahmed body, Grandemange et al. (2013a) showed that a decrease of the ground clearance height is related to a sharp change in base pressure for a critical value of $G/W = 0.06$. This indicates that both G/W and the underbody velocity, which changed with G/W , may influence the model rear pressure. The present study helps in separating these two effects by focusing on the influence of underbody velocity only. Fig. 7(b) gives color maps of C_p distribution over the model rear for selected values of λ . In most cases, the pressure distribution is far from homogeneous, which suggests to estimate the vertical and horizontal gradients of the base pressure distribution. These estimates are defined by equation (2) where $\langle \overline{C_p} \rangle_j$ corresponds to a spatial average on three points of line j depicted in Fig. 1(b):

$$\frac{\partial \langle \overline{C_p} \rangle}{\partial y^*} = \frac{\langle \overline{C_p} \rangle_1 - \langle \overline{C_p} \rangle_2}{l_y/H} \tag{2a}$$

$$\frac{\partial \langle \overline{C_p} \rangle}{\partial z^*} = \frac{\langle \overline{C_p} \rangle_3 - \langle \overline{C_p} \rangle_4}{l_z/H} \tag{2b}$$

The evolution of these pressure gradients with λ is provided in Fig. 8. The horizontal gradient remains small with respect to the values of the vertical gradient, which has been noticed earlier in similar configurations (Cadot et al., 2016; Chaligné, 2013; Grandemange et al., 2014; Gutierrez

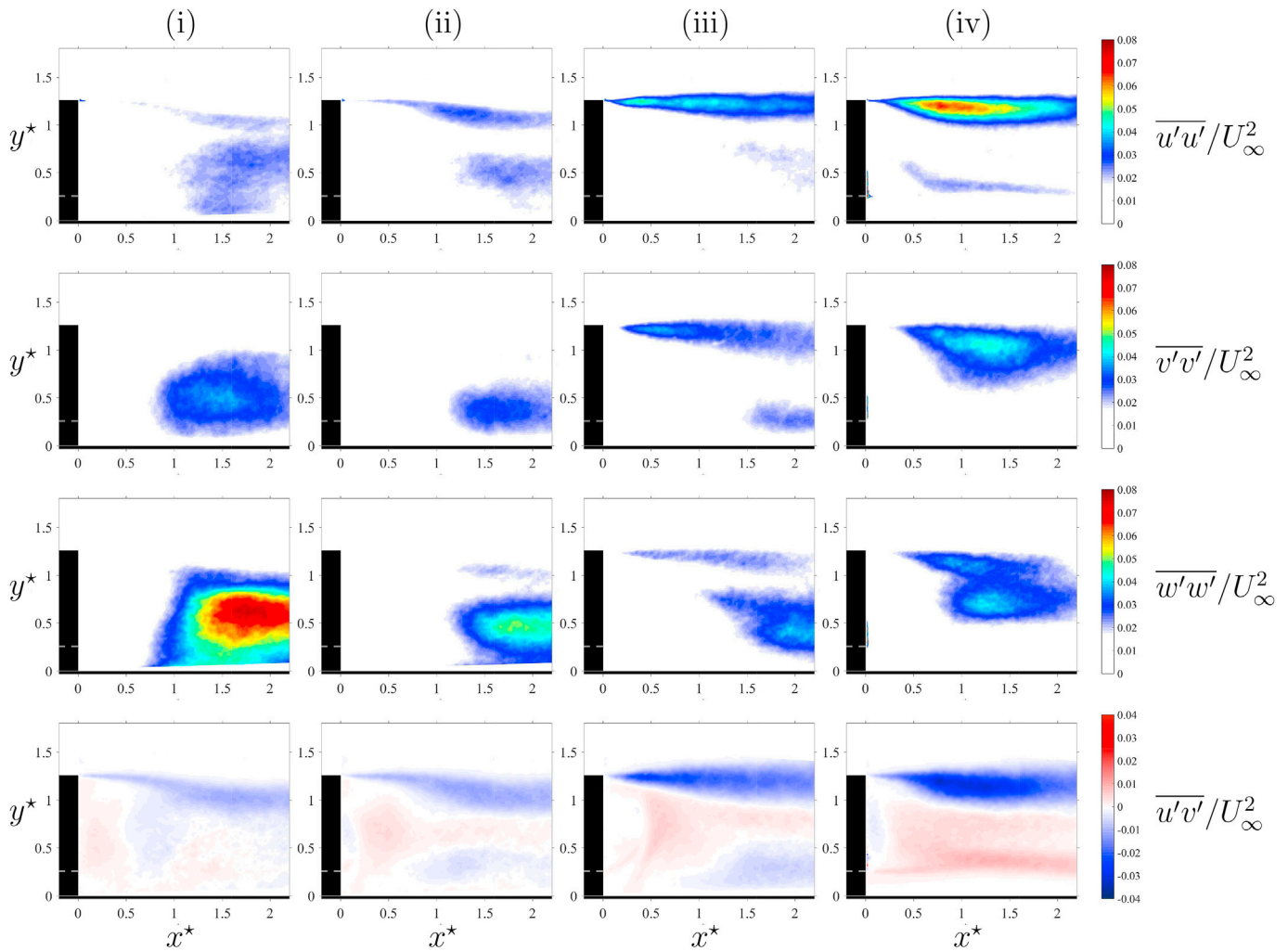


Fig. 13. Reynolds stresses in the mid plane for $\lambda =$ (i) 0.08, (ii) 0.21, (iii) 0.39, (iv) 0.86.

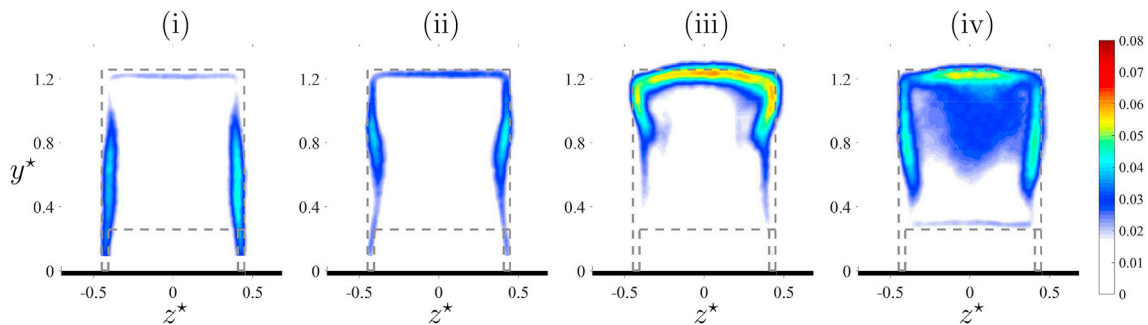


Fig. 14. Turbulent kinetic energy k^* in the $x^* = 0.5$ plane for $\lambda =$ (i) 0.08, (ii) 0.21, (iii) 0.39, (iv) 0.86.

et al., 1996; Szmigiel, 2017). The vertical gradient exhibits also a remarkable evolution with λ , being negative for very low values of the underbody velocity, peaking around 0.1 as λ reaches 0.25, and staging around 0.05 in a range of λ around 0.4. For larger values of λ , the vertical pressure gradient reaches high values again. This evolution denotes a strong influence of the underbody velocity on the near-wake and four flow classes can be distinguished. These classes, numbered from (I) to (IV) are reported on Figs. 7 and 8 together with vertical dashed lines as the estimated borders between classes. If the distinction between classes (I-II-III) and (IV) is related to a transition from a wake attached to the ground to a wake completely detached to the ground as for square-back

Ahmed body as later illustrated in section 4.2, the physical interpretation governing the differences between the classes (I), (II) and (III) is less obvious. In the following, complementary analyzes are presented to better characterize of these flow classes; results obtained in particular with four selected values of λ , corresponding to those used in Fig. 7(b), will be used to illustrate representative characteristics of each of the four classes identified above.

A first complement comes with the examination of the standard deviation of the pressure coefficient on the model rear. Its evolution with the underbody velocity is presented in Fig. 9. When λ increases, the location of the maximum of pressure fluctuations moves from the bottom

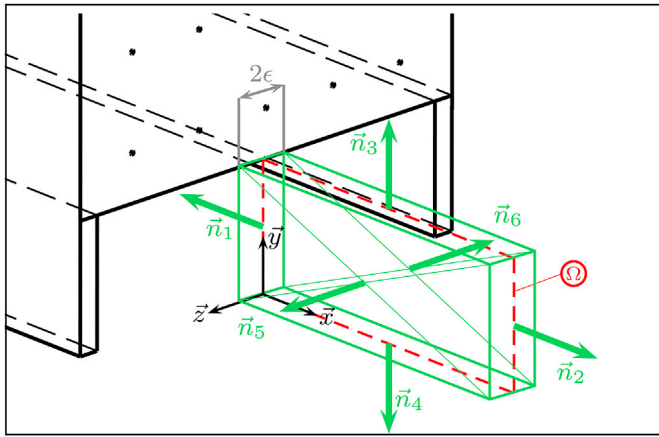


Fig. 15. Position of the closed control volume for establishing the momentum balance.

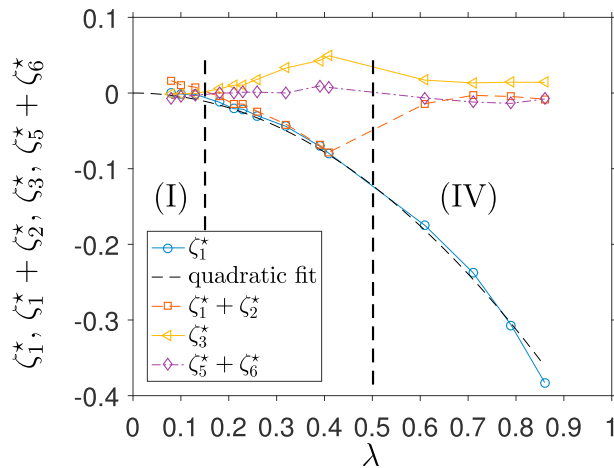


Fig. 16. Evolution with λ of the different momentum flux terms over the selected control volume.

to the top of the model rear. This result will be commented together with the analysis of the wake flow in section 4.2. The pressure fluctuations are also much larger for class (IV), as illustrated considering $\lambda = 0.86$. Bistability has been previously seen in the case $H/W > 1$ (Grandemange et al., 2013b), for values of C/W typically greater than 0.4. The result obtained here is somewhat different, because the first signs of possible bistability (not illustrated here) have been encountered only for the maximum of λ in the present set-up, $\lambda = 0.86$. For the different configurations tested here, the base pressure gradient remains positive. It is likely that, for greater values of λ , results consistent with what obtained in (Grandemange et al., 2013b) for $C/W > 0.4$ would have been observed.

4.2. Mean flow

SPIV measurements have been performed in the 14 configurations corresponding to the different λ values used here. Fig. 10 gives the mean velocity fields obtained in the mid plane of the model for the values of λ representative of the flow classes identified above. First, a major distinction can be drawn between class (IV) where the underbody flow momentum is sufficient to be convected along the ground without separation, and classes (I-II-III), where the underbody flow forms a back-flow directed towards the base with separation from the ground. The results obtained here correspond to a fixed ground configuration, and are

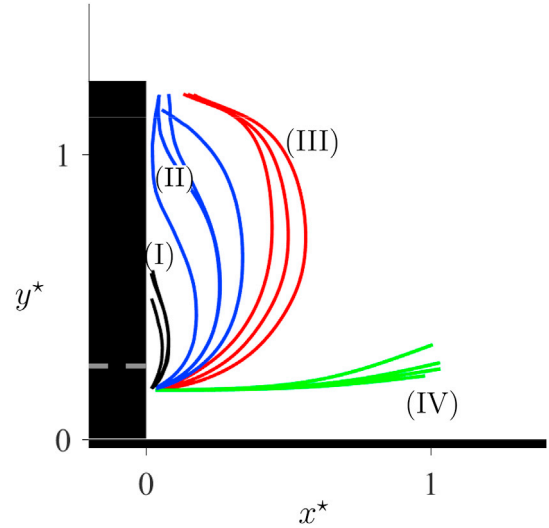


Fig. 17. Streamline starting at $(x^*, y^*) = (0.03, 0.2)$ for different values of λ .

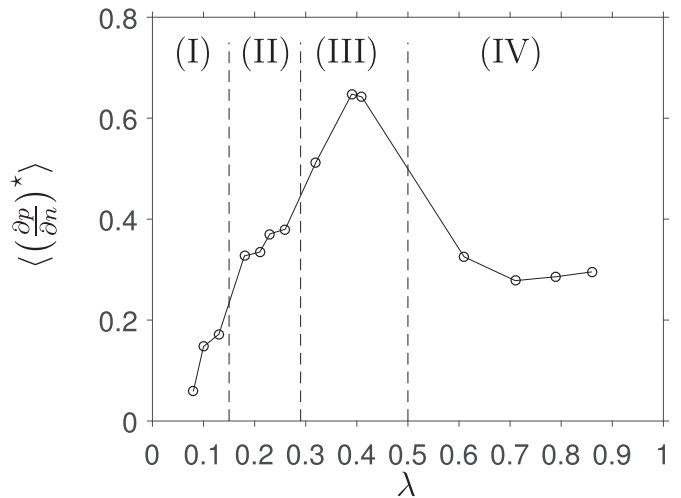


Fig. 18. Evolution with λ of the different contributions to the momentum balance over the selected control volume.

Table 1
Boundary layer characteristics at $x^* = -0.07$ in the mid plane.

λ	δ_{99} (mm)	δ (mm)	θ_0 (mm)	Re_{θ_0}	h
0.08	18.1	1.96	1.59	2743	1.23
0.21	18.6	2.01	1.64	2810	1.22
0.32	17.9	1.95	1.60	2712	1.22
0.39	18.2	2.01	1.64	2795	1.23
0.41	17.7	2.00	1.63	2781	1.22
0.61	17.3	1.94	1.59	2694	1.22
0.86	16.6	1.92	1.55	2651	1.24

likely to be modified in the realistic case of a moving ground. Nevertheless, the same evolution of the wake characteristics with λ is expected, with a transition from one class to another possibly obtained at different values of λ . The following analyzes will focus on the flow topology in the vicinity of the base, less sensitive to the moving/fixed ground condition than the wake further downstream.

- For class (I), the wake in the mid plane is nearly similar to that of a 3D backward facing step flow with one main clockwise recirculation bubble attached to the ground, whose center denoted by A is depicted

Table 2

Boundary layer characteristics at $x^* = -0.07$ at mid height on the side of the model.

λ	δ_{99} (mm)	δ (mm)	θ_0 (mm)	Re_{θ_0}	h
0.08	20.2	1.39	1.21	2014	1.15
0.86	21.0	1.69	1.46	2457	1.16

in Fig. 10(i). According to the boundary condition, separation and reattachment points S_G and R_G appear on the ground. R_G is located around $x^* = 1.5$ as previously observed on a wall-mounted parallelepiped with the same aspect ratio than the present study (Martinez and Tropea, 1993).

- For a higher momentum underbody flow corresponding to class (II), illustrated in Fig. 10(ii), A is progressively pushed away from the base by the backflow emanating from the underbody region. Additionally, a counterclockwise recirculating bubble of center B develops near the bottom edge of the base. A stagnation point S_B is located in the bottom part of the base, between the separation points S_L and S_U located respectively on the lower and upper edges of the base. The vertical size of the vortex corresponding to B is defined by the distance between S_L and S_B and is thus around $0.5H$.
- For class (III) depicted in Fig. 10(iii), a new clockwise recirculation bubble appears near the ground, whose center C is axially located between S_G and R_G . The stagnation point S_B is pushed upward, near S_U , and the vertical size of the vortex B trapped by the backflow scales approximately with $0.9H$. The existence, behind the base, of a vortex whose vertical size is around H , with strong curvature and velocities, potentially induces large low pressure values in the direction of B . Due to the proximity of B , the base is therefore largely contaminated by these low pressure values for class (III), in accordance with the mean wall pressure map shown in Fig. 7(b) for $\lambda = 0.39$. The reorganization of the mean flow structure, also marked with the disappearance of the vortex defined by A , coincides with a strong base pressure jump observed in Fig. 7(a) between classes (II) and (III).

The systematic existence of the structures of different types (A , B and C) for flow classes (I), (II) and (III) is illustrated in Fig. 11 that summarizes the results obtained with the different tested values for λ .

- For class (IV), as illustrated in Fig. 10(iv), the mean wake is formed in the mid plane by two counter-rotating vortices (whose centers are denoted D_1 and D_2) as observed in the wake of a classical Ahmed body as well as real square-back passenger cars or light commercial vehicles (Grandemange et al., 2014).

Maps of longitudinal velocity magnitude in the transverse $x^* = 0.5$ plane are presented in Fig. 12, together with the streamlines in this plane. The isoline $u^* = 0$ helps in identifying the flow area where the longitudinal velocity is negative. For classes (I) and (II), (Fig. 12(i,ii)), this area spreads from the floor to half the model height and is associated with the back-flow coming from the upper shear layer. For class (III) as depicted in Fig. 12(iii), this area is located in the upper part of the model wake and corresponds to the region where the underbody flow is directed toward the model rear. For class (IV), illustrated in Fig. 12(iv), the recirculation area with two non-symmetric recirculation bubbles dictates the form of the $u^* < 0$ zone. Concerning the pattern of the streamlines, class (I) is clearly linked with streamlines going toward the sides of the lower part of the recirculating area, which indicates that the spanwise component of the mean velocity dominates in this region. Additionally, a rolling-up of the streamlines in the upper part of the near wake is noticed. On the contrary, for classes (II) and (III), the streamlines are oriented vertically on a large part of the near wake width, which corresponds to the underbody flow. Classes (II) and (III) mainly differ by the size of rolling-up of the streamlines in the upper part of the near wake and by the velocity magnitude in the underbody region. For class (IV), illustrated in

Fig. 12(iv), the rolling-up of the streamlines is moved toward the lower part of the near wake.

4.3. Turbulence in the near wake

Time-averaged Reynolds stresses derived from spiv measurements in the mid plane are given in Fig. 13. For classes (I) and (II), the normal Reynolds stress $\overline{w'w'}$ is the dominant component and is concentrated around $x^* \approx 1.7$ at mid-height of the model. The high values of $\overline{w'w'}$ are related to strong lateral flow movements at the closure of the main vortex A . High levels of $\overline{v'v'}$ are also located in the same area. On the other hand, for classes (III) and (IV), the main contributor to turbulent kinetic energy is the normal Reynolds stress $\overline{u'u'}$ localized inside the upper shear layer, as observed on an Ahmed body (Barros et al., 2016; Grandemange et al., 2013b). For a given diagonal term of the Reynolds stress tensor ($\overline{u'u'}$, $\overline{v'v'}$, or $\overline{w'w'}$), an increase in λ leads to a decrease of its intensity in the lower region of the model wake, and an increase in the upper part of the model wake. The $\overline{u'u'}$ term reinforces with λ and is more intense in the upper shear layer.

Turbulent kinetic energy k^* measured in the transverse plane at $x^* = 0.5$ is presented in Fig. 14. It is noteworthy that the largest velocity fluctuations are confined inside the lateral shear layers for classes (I) and (II), while they are shifted inside the upper shear layer for class (III). In this case, the interaction between the upper shear layer and the underbody flow redirected towards the model base, as observed in Fig. 10(iii), causes the increase in k^* . For class (IV), high levels of velocity fluctuations are located inside the upper and lateral shear layers, and turbulence intensity is also increased in a large part of the closed recirculating bubble as observed for the base pressure fluctuations in Fig. 9. The velocity fluctuations in the lower shear layer are small for all classes of flow compared to the turbulence generated by other shear layers. Thus, peculiarities related to the identified flow classes are also qualitatively identified through turbulence intensities in a given transversal plane. Complementary spectral analyzes would help in clarifying the interaction between the back-flow and the upper shear layer for class (III) and the physical origin of large transverse velocity fluctuations downstream the main recirculation bubble for class (I). A more general distinction between the flow classes is now sought from the mean flow properties viewpoint.

4.4. Analysis of momentum flux terms and pressure gradients

The objective is to propose a quantitative analysis of the wake characteristics that helps in discriminating the classes identified from rear pressure measurements, and especially classes (I), (II) and (III). Appropriate metrics based on the velocity fields in the different configurations studied are now considered.

First, the momentum flux terms related to the time averaged velocity field are estimated over a closed volume centered around the mid-plane Ω . This volume, depicted in Fig. 15 has a length l along \vec{x} and a width 2ϵ . The length l is chosen here to be half the model height H , but the conclusions presented here have been checked to be weakly dependent on l around this value. The bottom of the control volume coincides with the wind tunnel floor. The projection along \vec{x} of the momentum flux through a surface Ω_i of normal vector \vec{n}_i is noted ζ_i and expressed by:

$$\zeta_i = \left(\iint_{\Omega_i} \rho \vec{u} \left(\vec{u} \cdot \vec{n}_i \right) ds \right) \cdot \vec{x} \quad (3)$$

The term ζ_4 is zero because of the location of Ω_4 on the wind tunnel floor. For practical reasons, the terms ζ_5 and ζ_6 are combined:

$$\zeta_5 + \zeta_6 = \iint_{\Omega_5} \rho \vec{u}(x, y, z = \epsilon) \vec{w}(x, y, z = \epsilon) dx dy$$

$$-\iint_{\Omega_6} \rho \bar{u}(x, y, z = -\varepsilon) \bar{w}(x, y, z = -\varepsilon) dx dy$$

and simplifying assumptions are considered to approximate the different momentum flux terms. First, the plane Ω is supposed to be a plane of symmetry for the time-averaged velocities. As a consequence, the following properties are obtained:

$$\bar{w}(x, y, z = 0) = 0 \tag{4a}$$

$$\frac{\partial \bar{u}}{\partial z}(x, y, z = 0) = 0 \tag{4b}$$

Secondly, the width 2ε of the control volume is supposed to be small enough to allow for a first order Taylor expansion of the velocity field around the mid-plane. Therefore:

$$\bar{w}(x, y, z = \varepsilon) - \bar{w}(x, y, z = -\varepsilon) \sim 2\varepsilon \frac{\partial \bar{w}}{\partial z}(x, y, z = 0) \tag{5}$$

Consequently the sum of ζ_5 and ζ_6 is approximated by:

$$\zeta_5 + \zeta_6 \sim 2\varepsilon \iint_{\Omega} \rho \bar{u}(x, y, z = 0) \frac{\partial \bar{w}}{\partial z}(x, y, z = 0) dx dy \tag{6}$$

The term $\frac{\partial \bar{w}}{\partial z}(x, y, z = 0)$ in eq. (6) is not measured directly, but can be estimated with help of the continuity equation and the $SPIV$ data in the mid-plane (Ω). The terms ζ_i as defined in eq. (3) can be expressed in a condensed form, noted ζ_i^* , obtained by use of a reference momentum $\frac{1}{2}\rho U_\infty^2$ and a reference surface $H \times 2\varepsilon$, as follow:

$$\zeta_i^* = \frac{\zeta_i}{\frac{1}{2}\rho U_\infty^2 H \times 2\varepsilon} \tag{7a}$$

$$\zeta_1^* \sim -2 \int_0^{G^*} \overline{u^{*2}}(0, y^*) dy^* \tag{7b}$$

$$\zeta_2^* \sim 2 \int_0^{G^*} \overline{u^{*2}}(I^*, y^*) dy^* \tag{7c}$$

$$\zeta_3^* \sim 2 \int_0^{I^*} \overline{u^* v^*}(x^*, G^*) dx^* \tag{7d}$$

$$\zeta_5^* + \zeta_6^* \sim 2 \int_0^{I^*} \int_0^{G^*} \overline{u^* \frac{\partial w^*}{\partial z}} dx^* dy^* \tag{7e}$$

The terms listed in equation (7) are evaluated for different values of λ , and their corresponding evolution is presented in Fig. 16. The term ζ_1^* represents the momentum flux of the underbody flow at the model rear; its evolution with λ is quadratic as expected. The examination of $(\zeta_1^* + \zeta_2^*)$ is suitable for different purposes. For $\lambda < 0.15$, which corresponds to the range previously identified from pressure measurements as that of class (I), ζ_1^* is almost zero, while the sum $(\zeta_1^* + \zeta_2^*)$ is positive. Thus, it corresponds to configurations where a large clockwise recirculation bubble A exists, typical of class (I). For larger values of λ , this sum is negative and its value is close to that of ζ_1^* , which corresponds to configurations where the momentum flux at the model rear is significantly higher than that through the control surface Ω_2 . In these cases, the gradual increase of ζ_3^* with λ is explained by the increase of the vertical back-flow intensity due to the backflow forming a curved jet and the separation from the ground. For $\lambda > 0.5$, $(\zeta_1^* + \zeta_2^*)$ reaches zero while ζ_3^* and $\zeta_5^* + \zeta_6^*$ remain small: this corresponds to configurations where the momentum flux at the model rear is preserved up to the control surface Ω_2 , which is a property typical of class (IV). It is noteworthy that the sum $(\zeta_5^* + \zeta_6^*)$ is significantly smaller than the other terms over the range of λ tested, which indicates that it could reasonably be neglected. It is shown here for completeness purposes. As a summary, the momentum budget allows here to discriminate class (I), where $\zeta_1^* + \zeta_2^*$ is positive, from class (IV), where $\zeta_1^* + \zeta_2^*$ is zero; in-between, a region where $\zeta_1^* + \zeta_2^*$ is negative while ζ_3^* is positive exists, and corresponds to classes (II) and (III). At this stage, it is

not possible to discriminate between classes (II) and (III) using only the analysis of the momentum terms. A further metric is required to distinguish these two classes by use of quantitative flow analyzes.

The main differences between classes (II) and (III) are the magnitude and the curvature of the back-flow which forms at the underbody exit and impinges the base as exhibited in Fig. 10(ii), or the upper shear layer as depicted in Fig. 10(iii). To illustrate this effect of curvature, the streamline starting at $(x^*, y^*) = (0.03, 0.2)$, thus in the underbody flow, is plotted in Fig. 17 for the different values of λ considered. For classes (II) and (III), the marked curvature of the streamlines is suspected to induce a negative pressure gradient in the direction of the base, particularly for class (III) where the sign of the curvature is constant from the bottom to the top of the considered streamlines.

Thus, the local normal pressure gradient $\left(\frac{\partial p}{\partial n}\right)^*$ related to the streamline curvature in the mid-plane is estimated by use of equation (8):

$$\left(\frac{\partial p}{\partial n}\right)^* = 2 \frac{U^{*2}}{R^*} \tag{8}$$

where R is the local radius of curvature of the streamline. To limit the effects of measurement noise in the computation of R which involves second derivatives, the pressure gradient is averaged along the streamline up to the point where the local streamline angle with respect to the x direction is maximum. This angle corresponds to 90° in the cases where the underbody flow impinges the base. The result $\left\langle \left(\frac{\partial p}{\partial n}\right)^* \right\rangle$ is presented in

Fig. 18. This quantity is very small for class (I). For classes (II) and (IV), it remains around 0.35. A large increase up to 0.65 is obtained for class (III) around $\lambda = 0.4$, which allows to efficiently discriminate between classes (II) and (III). It is remarkable that, despite the three dimensional character of the flow, a classification of the different flow structures can be derived with two simple indicators (flow momentum and pressure gradient) using the mean velocity field in a 2D vertical slice only.

5. Conclusion

In the present study, a simplified square-back tractor-trailer model of scale 1:43 is studied at a Reynolds number of 1.3×10^5 . This model allows the ratio λ between the underbody velocity and the free stream velocity to be varied from 0.08 to 0.86, with the objective of identifying the effect of this single parameter on the near wake structure. The flow at the nose and upstream the separation point at the model rear is first characterized, and the boundary layer characteristics on the roof and the side walls are shown to be weakly influenced by λ . This ensures that modifications of the near wake by changing λ are not due to a disruption of the incoming flow conditions.

A first result of this study is that the variation of the underbody velocity at a constant ground clearance leads to various wake topologies. A classification between the different wakes for various λ has been made, leading to a distinction between four different flow classes that have different salient features. For class (I), high levels of transverse velocity fluctuations are noticed, and the momentum flux term $\zeta_1 + \zeta_2$ is strictly positive. Other peculiarities for class (I) correspond to a wake exhibiting a recirculating bubble in the upper part of the model base, and a very small base pressure vertical gradient. On the contrary, class (II) is characterized by high values of the base pressure vertical gradient together with high mean base pressure levels and a back flow phenomenon from the underbody region to the model base. For class (III), the intensity of the back-flow is high, which induces a large increase in the in-flow pressure gradient directed toward the model base. This feature is in-line with the decrease of the mean base-pressure noticed for configurations related to class (III). Furthermore in this case, the stagnation point on the model base is very close to the base top, and a new wake structure comprising a recirculating bubble located near the ground is observed. Finally, class

(IV) is characterized by the presence, in the model mid-plane, of two contra-rotating bubbles detached from the ground, as in previous studies of Ahmed body or GTS/GETS models. These different flow classes are in qualitative agreement with those derived from an earlier study (McArthur et al., 2016), in which the ground clearance only has been changed.

The existence of a back-flow appears to be a salient feature of the wake for full-scale heavy trucks, for which λ is likely to be small and remains typically lower than 0.5 even with a moving ground condition, as one consequence of the small gap between the tractor and the road, which will limit the flux under the trailer. In more realistic configurations, e.g. when taking the underride guard into account, the underbody flux is even more reduced. For trucks aerodynamics, the identification of the limit between class (II) and class (III) configurations is of practical interest; in this case, the difference in underbody flux may be small but the difference in mean base pressure significant.

Thus, GTS/GETS models used with a too large value of the ground clearance height are not appropriate to represent the wake of a heavy duty because of a non-realistic near-wake induced by a too high underbody velocity. The interpretation of the flow classes properties with respect to the possible existence of bifurcation and symmetry breaking

modes, as studied in (Grandemange et al., 2013b) for instance, is of primary interest, and may require further experiments at various ground clearance heights. The identification of flow classes and their related properties are helpful to define the appropriate operating conditions for the application of control strategies (using flaps or fluidic control) to increase the mean base pressure, and reduce the drag of heavy-duty vehicles in practical applications.

Acknowledgements

This work was performed within the framework of the Labex CeLyA of the Université de Lyon, within the programme "Investissements d'Avenir" (ANR-10-LABX-0060/ANR-11-IDEX-0007) operated by the French National Research Agency (ANR). The funding of ANRT (CIFRE grant 2013/1446 with Renault Trucks) for the PhD thesis of M.Szmigiel is gratefully acknowledged. The authors wish to thank J.M. Perrin, E.Jon-deau, N.Grosjean and P.Souchotte for their technical support during the experiments; the help of C.Sicot (Pprime) with the pressure scanner is also acknowledged.

Appendix A

The boundary layer thickness δ_{99} , the displacement thickness δ , the momentum thickness θ_0 , the shape factor $h = \delta/\theta_0$ and the Reynolds number Re_{θ_0} are given for several values of λ , in Table 1 for the boundary layer on the roof and in Table 2 for the boundary layer on a side wall. The momentum thickness is smaller on the side wall than on the roof, which is attributed to the limited flow separation effect at the model nose. The momentum thickness is more dependent on λ on the side wall than on the roof, which may be due to the disturbances located at the model front in the cases of small λ values.

References

- Ahmed, S.R., Ramm, G., Faltin, G., 1984. Some salient features of the time-averaged ground vehicle wake. SAE Int. Congr. Expo. <https://doi.org/10.4271/840300>, 840300.
- Barros, D., Boré, J., Noack, B.R., Spohn, A., Ruiz, T., 2016. Bluff body drag manipulation using pulsed jets and coanda effect. J. Fluid Mech. 805, 422–459.
- Basara, B., 2015. Fluid flow and conjugate heat transfer in a matrix of surface-mounted cubes: a PANS study. Int. J. Heat Fluid Flow 51, 166–174. <https://doi.org/10.1016/j.ijheatfluidflow.2014.10.012>.
- Bonnaïon, G., Cadot, O., Évrard, A., Herbert, V., Détery, J., 2017. On multistabilities of real car's wake. J. Wind Eng. Ind. Aerod. 164, 22–33.
- Cadot, O., Courbois, A., Ricot, D., Ruiz, T., Harambat, F., Herbert, V., Vigneron, R., Delery, J., 2016. Characterizations of force and pressure fluctuations on real vehicles. Int. J. Eng. Syst. Model Simulat. <https://doi.org/10.1504/IJESMS.2016.075529>.
- Chaligné, S., 2013. Contrôle du sillage d'un corps non profilé. Application expérimentale à une maquette simplifiée de véhicule industriel, Bluff-body wake control. Experimental application on a reduced-scale model of industrial vehicle. PhD Thesis. Université de Lyon, pp. 2013–2050. ECL - No.
- Croll, R.H., Gutierrez, W.T., Hassan, B., Suazo, J.E., Riggins, A.J., 1996. Experimental Investigation of the Ground Transportation Systems (GTS) Project for Heavy Vehicle Drag Reduction, SAE Technical Paper. <https://doi.org/10.4271/960907>.
- Garry, K.P., 1996. Some effects of ground clearance and ground plane boundary layer thickness on the mean base pressure of a bluff vehicle type body. J. Wind Eng. Ind. Aerod. 62, 1–10. [https://doi.org/10.1016/S0167-6105\(96\)00054-2](https://doi.org/10.1016/S0167-6105(96)00054-2).
- Grandemange, M., Gohlke, M., Cadot, O., 2013. Bi-stability in the turbulent wake past parallelepiped bodies with various aspect ratios and wall effects. Phys. Fluids 25. <https://doi.org/10.1063/1.4820372>.
- Grandemange, M., Gohlke, M., Cadot, O., 2013. Turbulent wake past a three-dimensional blunt body. Part 1. Global modes and bi-stability. J. Fluid Mech 722, 51–84. <https://doi.org/10.1017/jfm.2013.83>.
- Grandemange, M., Ricot, D., Vartanian, C., Ruiz, T., Cadot, O., 2014. Characterisation of the flow past real road vehicles with blunt afterbodies. Int. J. Aerodyn 4 (1/2), 24–42.
- Grandemange, M., Cadot, O., Courbois, A., Herbert, V., Vigneron, R., 2015. A study of wake effects on the drag of Ahmed's squareback model at the industrial scale. J. Wind Eng. Ind. Aerod. 145, 282–291.
- Gutierrez, W.T., Hassan, B., Robert, H., 1996. Aerodynamics overview of the ground transportation systems (GTS) project for heavy vehicle drag reduction. SAE Int. Congr. Expo. <https://doi.org/10.4271/960906>, 960906.
- Hwang, B.G., Lee, S., Lee, E.J., Kim, J.J., Lee, S.J., 2016. Reduction of drag in heavy vehicles with two different types of advanced side skirts. J. Wind Eng. Ind. Aerod. 155, 36–46.
- Islam, A., Gaylard, A., Thornber, B., 2017. A detailed statistical study of unsteady wake dynamics from automotive bluff bodies. J. Wind Eng. Ind. Aerod. 171, 161–177.
- Klebanoff, P.S., 1955. Characteristics of Turbulence in a Boundary Layer with Zero Pressure Gradient. NACA-TR-1247.
- Krajnovic, S., Davidson, L., 2015. Influence of floor motions in wind tunnels on the aerodynamics of road vehicles. J. Wind Eng. Ind. Aerod. 93, 677–696.
- Kowata, S., Ha, J., Yoshioka, S., Kato, T., Kohama, Y., 2008. Drag force reduction of a bluff-body with an underbody slant and rear flaps. SAE Int. J. Commer. Veh 1, 230–236. <https://doi.org/10.4271/2008-01-2599>.
- Littlewood, R.P., Passmore, M.A., 2012. Aerodynamic drag reduction of a simplified squareback vehicle using steady blowing. Exp. Fluid 53, 519–529. <https://doi.org/10.1007/s00348-012-1306-4>.
- Martinuzzi, R., Tropea, C., 1993. The flow around surface-mounted, prismatic obstacles placed in a fully developed channel flow (data bank contribution). J. Fluid Eng. 115, 85. <https://doi.org/10.1115/1.2910118>.
- McArthur, D., Burton, D., Thompson, M., Sheridan, J., 2016. On the near wake of a simplified heavy vehicle. J. Fluid Struct. 66, 293–314. <https://doi.org/10.1016/j.jfluidstruct.2016.07.011>.
- Nakashima, T., Tsubokura, M., Nouzawa, T., Nakamura, T., Zhang, H., Oshima, N., 2008. Large-eddy Simulation of Unsteady Vehicle Aerodynamics and Flow Structures, Bluff Bodies Aerodynamics & Applications (BBAA VI) International Colloquium, Milano, Italy, pp. 20–24. July.
- Perry, A.-K., Passmore, M.A., 2013. The impact of underbody roughness on rear wake structure of a squareback vehicle. SAE Tech. Pap. <https://doi.org/10.4271/2013-01-0463>, 2013-01-04.
- Salati, L., Schito, P., Cheli, F., 2017. Wind tunnel experiment on a heavy truck equipped with front-rear trailer device. J. Wind Eng. Ind. Aerod. 171, 101–109.
- Storms, B.L., Ross, J.C., Heineck, J.T., Walker, S.M., Driver, D.M., Zilliac, G.G., 2001. An Experimental Study of the Ground Transportation System (GTS) Model in the NASA Ames 7- by 10-Ft Wind Tunnel. NASA/TM-2001-209621.
- Szmigiel, M., Castelain, T., Michard, M., Juvé, D., Chacaton, D., 2016. Impact of the Underside Velocity on the Drag Reduction of a Trailer Model Using a Passive Control System, Aerovehicles II, Göteborg, Sweden. June 21–23.
- Szmigiel, M., 2017. Effet du flux de soubassement sur la dynamique du sillage d'un corps non profilé à culot droit. Application du contrôle actif pour la réduction de traînée de véhicule industriel, Effect of the underbody flux on square-back body-wake dynamics. Application of active control to drag reduction on an industrial vehicle. PhD thesis. Université de Lyon, 2017LYSEC16.
- Uffinger, T., Ali, I., Becker, S., 2013. Experimental and numerical investigations of the flow around three different wall-mounted cylinder geometries of finite length. J. Wind Eng. Ind. Aerod. 119, 13–27.
- Van Raemdonck, G.M.R., Van Tooren, M.J.L., 2008. Time-averaged Phenomenological Investigation of a Wake behind a Bluff Body, Bluff Bodies Aerodynamics & Applications (BBAA VI) International Colloquium, Milano, Italy, pp. 20–24. July.